

spans in this study, the effect of increased levels of IGF-1 by RJ/pRJ treatment on life span was not clear. However, previous studies reported that RJ/pRJ extended the life span in mice and *Caenorhabditis elegans* (10,11). Further studies are required to evaluate the effects and mechanisms of RJ/pRJ on life span.

Dietary supplementation with 1%–5% RJ/pRJ would be too great in an amount and would not be feasible for humans. Generally, dietary supplementation intake in animals cannot be directly converted into human dietary intake. Thus, we did a pilot study to examine the effect of RJ on muscle strength and physical performance in free-living elderly patients (Identifier: UMIN000004057, Trial Registration: <http://www.umin.ac.jp/ctr/index.htm>). We found that the intake of RJ (low dose: 1.2 g/day; high dose: 4.8 g/day) for 3 months improved muscle strength and physical performance in the elderly patients. Based on this pilot study, we are performing a randomized, double-blinded, placebo-controlled trial to confirm the effects of RJ on muscle strength and physical performance of the elderly patients (Identifier: UMIN000009648, Trial Registration: <http://www.umin.ac.jp/ctr/index.htm>).

In conclusion, in vivo, RJ/pRJ treatment increased the muscle weight, grip strength, regenerating capacity of injured muscles, and serum IGF-1 levels compared with controls in aged mice. In vitro, pRJ increased the cell proliferation rate, promoted the cell differentiation, and activated Akt-signaling pathway compared with controls in isolated satellite cells from aged mice. These findings suggest that RJ/pRJ treatment may have a beneficial effect on the prevention of age-related sarcopenia through increasing the systemic IGF-1 levels and activating Akt-signaling pathways in satellite cells.

#### FUNDING

This research was supported by Yamada Research Grant.

#### CONFLICT OF INTERESTS

All the authors have no conflicts of interest to disclose.

#### REFERENCES

- Nations United. *Department of Economic and Social Affairs Population Division: World Population Ageing 2009*. New York: United Nations; 2009:11.
- Altun M, Grönholdt-Klein M, Wang L, Ulfhake B. Cellular degradation machineries in age-related loss of muscle mass (Sarcopenia). In: Nagata T, ed. *Senescence*. San Francisco, CA: Academia.edu; 2012:269–286.
- Hawke TJ, Garry DJ. Myogenic satellite cells: physiology to molecular biology. *J Appl Physiol*. 2001;91:534–551.
- Clemmons DR. Role of IGF-1 in skeletal muscle mass maintenance. *Trends Endocrinol Metab*. 2009;20:349–356.
- Welle S. Cellular and molecular basis of age-related sarcopenia. *Can J Appl Physiol*. 2002;27:19–41.
- Sacco A, Doyonnas R, Kraft P, Vitorovic S, Blau HM. Self-renewal and expansion of single transplanted muscle stem cells. *Nature*. 2008;456:502–506.
- Giovannini S, Marzetti E, Borst SE, Leeuwenburgh C. Modulation of GH/IGF-1 axis: potential strategies to counteract sarcopenia in older adults. *Mech Ageing Dev*. 2008;129:593–601.
- Viuda-Martos M, Ruiz-Navajas Y, Fernández-López J, Pérez-Alvarez JA. Functional properties of honey, propolis, and royal jelly. *J Food Sci*. 2008;73:R117–R124.
- Sabatini AG, Marcazzan GL, Caboni MF, Bogdanov S, Almeida-Muradian LB. Quality and standardisation of Royal Jelly. *J ApiProduct ApiMedical Sci*. 2009;1:1–6.
- Inoue S, Koya-Miyata S, Ushio S, Iwaki K, Ikeda M, Kurimoto M. Royal Jelly prolongs the life span of C3H/HeJ mice: correlation with reduced DNA damage. *Exp Gerontol*. 2003;38:965–969.
- Honda Y, Fujita Y, Maruyama H, et al. Lifespan-extending effects of royal jelly and its related substances on the nematode *Caenorhabditis elegans*. *PLoS One*. 2011;6:e23527.
- Kamakura M, Mitani N, Fukuda T, Fukushima M. Antifatigue effect of fresh royal jelly in mice. *J Nutr Sci Vitaminol (Tokyo)*. 2001;47:394–401.
- Matsui T, Yukiyoshi A, Doi S, Sugimoto H, Yamada H, Matsumoto K. Gastrointestinal enzyme production of bioactive peptides from royal jelly protein and their antihypertensive ability in SHR. *J Nutr Biochem*. 2002;13:80–86.
- Vitek J. Effect of royal jelly on serum lipids in experimental animals and humans with atherosclerosis. *Experientia*. 1995;51:927–935.
- Liu JR, Yang YC, Shi LS, Peng CC. Antioxidant properties of royal jelly associated with larval age and time of harvest. *J Agric Food Chem*. 2008;56:11447–11452.
- Kohno K, Okamoto I, Sano O, et al. Royal jelly inhibits the production of proinflammatory cytokines by activated macrophages. *Biosci Biotechnol Biochem*. 2004;68:138–145.
- Macaluso A, De Vito G. Muscle strength, power and adaptations to resistance training in older people. *Eur J Appl Physiol*. 2004;91:450–472.
- Strasser EM, Wessner B, Roth E. Cellular regulation of anabolism and catabolism in skeletal muscle during immobilisation, aging and critical illness. *Wien Klin Wochenschr*. 2007;119:337–348.
- Schaap LA, Pluijm SM, Deeg DJ, Visser M. Inflammatory markers and loss of muscle mass (sarcopenia) and strength. *Am J Med*. 2006;119:526.e9–526.17.
- Meng SJ, Yu LJ. Oxidative stress, molecular inflammation and sarcopenia. *Int J Mol Sci*. 2010;11:1509–1526.
- Sriram S, Subramanian S, Sathiakumar D, et al. Modulation of reactive oxygen species in skeletal muscle by myostatin is mediated through NF- $\kappa$ B. *Aging Cell*. 2011;10:931–948.
- Okazaki T, Ebihara S, Asada M, et al. Macrophage colony-stimulating factor improves cardiac function after ischemic injury by inducing vascular endothelial growth factor production and survival of cardiomyocytes. *Am J Pathol*. 2007;171:1093–1103.
- Yahiaoui L, Gvozdic D, Danialou G, Mack M, Petrof BJ. CC family chemokines directly regulate myoblast responses to skeletal muscle injury. *J Physiol*. 2008;586:3991–4004.
- Okazaki T, Ebihara S, Asada M, Yamanda S, Niu K, Arai H. Erythropoietin promotes the growth of tumors lacking its receptor and decreases survival of tumor-bearing mice by enhancing angiogenesis. *Neoplasia*. 2008;10:932–939.
- Nakajima R, Takao K, Huang SM, et al. Comprehensive behavioral phenotyping of calpastatin-knockout mice. *Mol Brain*. 2008;7:1–15.
- Uezumi A, Fukada S, Yamamoto N, Takeda S, Tsuchida K. Mesenchymal progenitors distinct from satellite cells contribute to ectopic fat cell formation in skeletal muscle. *Nat Cell Biol*. 2010;12:143–152.
- Niu K, Asada M, Okazaki T, et al. Adiponectin pathway attenuates malignant mesothelioma cell growth. *Am J Respir Cell Mol Biol*. 2012;46:515–523.
- Fukada S, Yamaguchi M, Kokubo H, et al. Hes1 and Hes3 are essential to generate undifferentiated quiescent satellite cells and to maintain satellite cell numbers. *Development*. 2011;138:4609–4619.
- Asada M, Ebihara S, Yamanda S, et al. Depletion of serotonin and selective inhibition of 2B receptor suppressed tumor angiogenesis by

- inhibiting endothelial nitric oxide synthase and extracellular signal-regulated kinase  $\frac{1}{2}$  phosphorylation. *Neoplasia*. 2009;11:408–417.
30. Yamada S, Ebihara S, Asada M, et al. Role of ephrinB2 in non-productive angiogenesis induced by Delta-like 4 blockade. *Blood*. 2009;113:3631–3639.
31. Okazaki T, Sakon S, Sasazuki T, et al. Phosphorylation of serine 276 is essential for p65 NF-kappaB subunit-dependent cellular responses. *Biochem Biophys Res Commun*. 2003;300:807–812.
32. Okazaki T, Ni A, Baluk P, et al. Capillary defects and exaggerated inflammatory response in the airways of EphA2-deficient mice. *Am J Pathol*. 2009;174:2388–2399.
33. Chevenne D, Porquet D. Growth hormone (GH) and insulin-like growth factor 1 (IGF-1) in nutritional status. *Ann Biol Clin (Paris)*. 1995;53:527–538.
34. Campillo B, Paillaud E, Bories PN, Noel M, Porquet D, Le Parco JC. Serum levels of insulin-like growth factor-1 in the three months following surgery for a hip fracture in elderly: relationship with nutritional status and inflammatory reaction. *Clin Nutr*. 2000;19:349–354.
35. Ponzer S, Tidermark J, Brismar K, Söderqvist A, Cederholm T. Nutritional status, insulin-like growth factor-1 and quality of life in elderly women with hip fractures. *Clin Nutr*. 1999;18:241–246.
36. McWhirter JP, Ryan MF, Pennington CR. An evaluation of insulin-like growth factor-1 as an indicator of nutritional status. *Clin Nutr*. 1995;14:74–80.
37. Kandarian SC, Jackman RW. Intracellular signaling during skeletal muscle atrophy. *Muscle Nerve*. 2006;33:155–165.
38. Carter CS, Ramsey MM, Ingram RL, et al. Models of growth hormone and IGF-1 deficiency: applications to studies of aging processes and lifespan determination. *J Gerontol A Biol Sci Med Sci*. 2002;57:B177–B188.
39. Chiba T, Yamaza H, Shimokawa I. Role of insulin and growth hormone/insulin-like growth factor-1 signaling in lifespan extension: rodent longevity models for studying aging and calorie restriction. *Curr Genomics*. 2007;8:423–428.

# Comparison of the binding characteristics of [<sup>18</sup>F]THK-523 and other amyloid imaging tracers to Alzheimer's disease pathology

Ryuichi Harada · Nobuyuki Okamura ·  
Shozo Furumoto · Tetsuro Tago · Masahiro Maruyama ·  
Makoto Higuchi · Takeo Yoshikawa · Hiroyuki Arai ·  
Ren Iwata · Yukitsuka Kudo · Kazuhiko Yanai

Received: 1 May 2012 / Accepted: 21 September 2012 / Published online: 26 October 2012  
© Springer-Verlag Berlin Heidelberg 2012

## Abstract

**Purpose** Extensive deposition of senile plaques and neurofibrillary tangles in the brain is a pathological hallmark of Alzheimer's disease (AD). Although several PET imaging agents have been developed for in vivo detection of senile plaques, no PET probe is currently available for selective detection of neurofibrillary tangles in the living human

**Electronic supplementary material** The online version of this article (doi:10.1007/s00259-012-2261-2) contains supplementary material, which is available to authorized users.

R. Harada · N. Okamura (✉) · S. Furumoto · T. Yoshikawa ·  
K. Yanai  
Department of Pharmacology,  
Tohoku University School of Medicine,  
2-1, Seiryomachi, Aoba-ku,  
Sendai 980-8575, Japan  
e-mail: nookamura@med.tohoku.ac.jp

S. Furumoto · T. Tago · R. Iwata  
Division of Radiopharmaceutical Chemistry,  
Cyclotron and Radioisotope Center, Tohoku University,  
Sendai, Japan

M. Maruyama · M. Higuchi  
Molecular Imaging Center, National Institute  
of Radiological Sciences,  
Chiba, Japan

H. Arai  
Department of Geriatrics and Gerontology, Institute of  
Development, Aging and Cancer, Tohoku University,  
Sendai, Japan

Y. Kudo  
Innovation of New Biomedical Engineering Center,  
Tohoku University,  
Sendai, Japan

brain. Recently, [<sup>18</sup>F]THK-523 was developed as a potential in vivo imaging probe for tau pathology. The purpose of this study was to compare the binding properties of [<sup>18</sup>F]THK-523 and other amyloid imaging agents, including PiB, BF-227 and FDDNP, to synthetic protein fibrils and human brain tissue.

**Methods** In vitro radioligand binding assays were conducted using synthetic amyloid  $\beta_{42}$  and K18 $\Delta$ K280-tau fibrils. Nonspecific binding was determined by the addition of unlabelled compounds at a concentration of 2  $\mu$ M. To examine radioligand binding to neuropathological lesions, in vitro autoradiography was conducted using sections of AD brain.

**Results** [<sup>18</sup>F]THK-523 showed higher affinity for tau fibrils than for A $\beta$  fibrils, whereas the other probes showed a higher affinity for A $\beta$  fibrils. The autoradiographic analysis indicated that [<sup>18</sup>F]THK-523 accumulated in the regions containing a high density of tau protein deposits. Conversely, PiB and BF-227 accumulated in the regions containing a high density of A $\beta$  plaques.

**Conclusion** These findings suggest that the unique binding profile of [<sup>18</sup>F]THK-523 can be used to identify tau deposits in AD brain.

**Keywords** PET probes · Tau · Amyloid · Alzheimer's disease

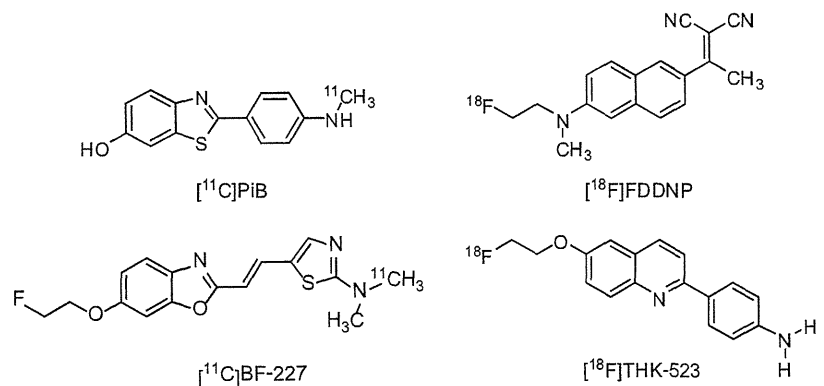
## Introduction

Senile plaques and neurofibrillary tangles (NFTs) composed of amyloid- $\beta$  (A $\beta$ ) peptides and aggregated tau proteins, respectively, are the pathological hallmarks of

Alzheimer's disease (AD). In vivo amyloid imaging techniques have received a lot of attention for their promise in presymptomatic detection of A $\beta$  pathology [1]. Recently, several  $\beta$ -sheet binding radiotracers have been developed as PET amyloid imaging agents [2]. Among them,  $^{18}\text{F}$ -labelled 2-(1-{6-[(2-fluoroethyl(methyl)amino)-2-naphthyl]ethylidene}malonitrile) ([ $^{18}\text{F}$ ]FDDNP) was the first PET probe to be applied to clinical PET imaging in patients with AD [3]. This tracer demonstrated higher regional uptake in the medial temporal lobe and neocortex, and was claimed to bind to A $\beta$  and tau pathological lesions [3]. Subsequently,  $^{11}\text{C}$ -labelled 2-[4'-(methylamino)phenyl]-6-hydroxybenzothiazole ([ $^{11}\text{C}$ ]PiB) and 2-(2-[dimethylaminothiazole-5-yl]ethenyl)-6-(2-[fluoro]ethoxy)benzoxazole ([ $^{11}\text{C}$ ]BF-227) were also developed as amyloid imaging radiotracers. These tracers bind to A $\beta$  fibrils with high affinity [4] and have demonstrated a significantly higher retention in the neocortical areas of brains of AD patients than of healthy controls [5, 6]. Furthermore, post-mortem analysis of AD patients who had undergone [ $^{11}\text{C}$ ]PiB PET imaging before death suggested a strong correlation between in vivo PiB binding and regional distribution of A $\beta$  plaques [7].

Amyloid imaging with PET can detect AD pathology in its preclinical stage [8]. However, amyloid deposition as assessed by [ $^{11}\text{C}$ ]PiB PET correlates poorly with cognitive impairment in AD [9, 10], whereas deposition of tau in the medial temporal cortex is closely associated with neuronal death in this region. Selective tau imaging would provide important information about the tau pathophysiological features in AD, allowing correlation of brain tau load with cognitive decline, monitoring of disease progression and evaluation of therapeutic efficacy of newly developed therapies. Potential candidates for in vivo tau imaging agents include quinoline derivatives [11], and in a recent study, we found that one quinoline derivative, [ $^{18}\text{F}$ ]THK-523, showed higher affinity for tau rather than amyloid fibrils. Furthermore, an autoradiography analysis indicated that this tracer binds specifically to tau deposits but not A $\beta$  burden at tracer concentrations usually achieved during a PET scan [12].

**Fig. 1** Chemical structures of [ $^{11}\text{C}$ ]PiB, [ $^{18}\text{F}$ ]FDDNP, [ $^{11}\text{C}$ ]BF-227 and [ $^{18}\text{F}$ ]THK-523



The binding profiles of PiB, BF-227 and FDDNP to A $\beta$  fibrils have been well described. Because tau,  $\alpha$ -synuclein and prion fibrils, as well as A $\beta$  fibrils, share a common  $\beta$ -sheet secondary structure, these compounds can potentially bind all these misfolded proteins. A previous study indicated that PiB binds to both A $\beta$  and PHF tau pathology in vitro [13]. However, the binding occurs at higher concentrations than usually achieved in vivo during a PET scan. Furthermore, PET–pathology correlation studies have demonstrated that PiB binding reflects A $\beta$  pathology [7, 14]. Newly developed  $^{18}\text{F}$ -labelled amyloid PET tracers have similarly shown good correlation with A $\beta$  plaque density [15, 16]. However, the binding affinity of these radiotracers for tau fibrils remains unknown and the binding properties of [ $^{18}\text{F}$ ]THK-523 have not been directly compared with those of other amyloid PET agents. Here, we compared the binding affinity of [ $^{18}\text{F}$ ]THK-523 to synthetic A $\beta$  and tau protein fibrils as well as to senile plaques and NFTs in human brain samples with those of PiB, BF-227 and FDDNP, to characterize the binding properties of THK-523 and to obtain a better understanding of current and future PET data.

## Materials and methods

### Materials

The nonlabelled compounds PiB, BF-227, FDDNP, THK-523 (Fig. 1) and their precursors were custom-synthesized by Tanabe R&D Service (Osaka, Japan). Human A $\beta_{42}$  was purchased from Peptide Institute Inc. (Mino, Japan). Recombinant K18 $\Delta$ K280-tau protein was obtained from Invitrogen (Tokyo, Japan).

### Radiolabelling of PiB, BF-227, THK-523 and FDDNP

[ $^3\text{H}$ ]PiB (specific activity 2.96 GBq/ $\mu\text{mol}$ ) was purchased from American Radiolabeled Chemicals (St. Louis, MO). [ $^{11}\text{C}$ ]PiB was radiolabelled using its precursor (2-(4-aminophenyl)-6-methoxymethoxybenzothiazole) and [ $^{11}\text{C}$ ]methyl triflate, as



previously described [17, 18]. The mean specific activity of [ $^{11}\text{C}$ ]PiB was 34.6 GBq/ $\mu\text{mol}$ .

[ $^{18}\text{F}$ ]BF-227 was synthesized by nucleophilic substitution of the tosylate precursor (2-[2-(2-dimethylaminothiazol-5-yl)ethenyl]-6-[2-(tosyloxy)ethoxy]benzoxazole. After a 10-min reaction at 110 °C, the crude mixture was partially purified on an activated Sep-Pak tC18 cartridge before being purified by semipreparative reverse-phase HPLC. Standard tC18 Sep-Pak reformulation produced [ $^{18}\text{F}$ ]BF-227 in >95 % purity. The radiochemical yield was 12–19 % (non-decay-corrected), and the mean specific activity of [ $^{18}\text{F}$ ]BF-227 was 163 GBq/ $\mu\text{mol}$  at the end of the synthesis. [ $^{11}\text{C}$ ]BF-227 was synthesized using *N*-desmethylated derivatives as its precursor and [ $^{11}\text{C}$ ]methyl triflate, as previously described [6]. The mean specific activity of [ $^{11}\text{C}$ ]BF-227 was 136 GBq/ $\mu\text{mol}$ .

[ $^{18}\text{F}$ ]THK-523 was synthesized by nucleophilic substitution of the tosylate precursor (2-(4-aminophenyl)-6-(2-tosyloxyethoxy)quinolone) as previously described [12]. The standard tC18 Sep-Pak reformulation produced [ $^{18}\text{F}$ ]THK-523 in >95 % purity. The radiochemical yield was 38–49 % (non-decay-corrected), and the mean specific activity of [ $^{18}\text{F}$ ]THK-523 was 68 GBq/ $\mu\text{mol}$  at the end of the synthesis.

[ $^{18}\text{F}$ ]FDDNP was radiolabelled by the nucleophilic substitution of the tosylate precursor (2-{[6-(2,2-dicyano-1-methylvinyl)-2-naphthyl](methyl)amino}ethyl-4-methylbenzenesulphonate) as previously described [19]. After a 15-min reaction at 95 °C, the crude mixture was partially purified on an activated Sep-Pak tC18 cartridge before being purified by semipreparative reverse-phase HPLC. Standard tC18 Sep-Pak reformulation produced [ $^{18}\text{F}$ ]FDDNP in >95 % purity. The radiochemical yield was 12–19 % (non-decay-corrected), and the mean specific activity of [ $^{18}\text{F}$ ]FDDNP was 27 GBq/ $\mu\text{mol}$  at the end of the synthesis. All analysis HPLC chromatograms are shown in the Supplementary figure.

#### In vitro radioligand binding assays

Synthetic A $\beta_{42}$  fibrils and K18 $\Delta$ K280-tau fibrils were prepared as previously described [12]. For in vitro binding assays, synthetic A $\beta_{42}$  or K18 $\Delta$ K280 fibrils (200 nM) were incubated with increasing concentrations of [ $^3\text{H}$ ]PiB and [ $^{18}\text{F}$ ]labelled compounds (0.5–200 nM). To account for nonspecific binding of [ $^3\text{H}$ ]PiB and [ $^{18}\text{F}$ ]labelled compounds, the above-mentioned reactions were performed in triplicate in the presence of each unlabelled compound at a concentration of 2  $\mu\text{M}$ .

The binding reactions were incubated for 1 h for the [ $^{18}\text{F}$ ]labelled compounds and 3 h for [ $^3\text{H}$ ]PiB at room temperature, in 200  $\mu\text{L}$  of assay buffer (Dulbecco's PBS, 0.1 % BSA). Separation of bound from free radioactivity was achieved by filtration under reduced pressure (MultiScreen HTS Vacuum Manifold, MultiScreen HTS 96-well 0.65- $\mu\text{m}$

filtration plate; Millipore, Billerica, MA). The filters were washed three times with 200- $\mu\text{L}$  assay buffer, and the filters containing the bound [ $^{18}\text{F}$ ]labelled compounds were then assayed for radioactivity in a  $\gamma$  counter (AccuFLEX  $\gamma$ 7000, Aloka, Tokyo, Japan). The filters containing [ $^3\text{H}$ ]PiB were incubated in 2 mL of scintillation fluid (Aquasol-2; PerkinElmer, Boston, MA), and the radioactivity of [ $^3\text{H}$ ]PiB was counted using a  $\beta$  counter (LS6500 liquid scintillation counter; Beckman Coulter, Brea, CA). The binding data were analysed with curve-fitting software that calculated the  $K_D$  and  $B_{\text{max}}$  using nonlinear regression (GraphPad Prism version 5.0; GraphPad Software, San Diego, CA).

Autoradiography, immunohistochemistry and Gallyas silver staining

Demographics of post-mortem brain samples are shown in Table 1. The frontal and medial temporal brain sections (6  $\mu\text{m}$  thick) of three AD patients were incubated with 1.0 MBq/mL [ $^{11}\text{C}$ ]labelled and [ $^{18}\text{F}$ ]labelled compounds at room temperature for 10 min and then washed briefly with water and 50 % ethanol. After drying, the labelled sections were exposed to a BAS-III imaging plate (Fuji Film, Tokyo, Japan) overnight. The autoradiographic images were obtained using a BAS-5000 phosphoimaging instrument (Fuji Film) with a spatial resolution of 25 $\times$ 25  $\mu\text{m}$ . The adjacent sections were immunostained using AT8 anti-tau monoclonal antibody (diluted 1:20; Innogenetics, Ghent, Belgium) and 6F/3D (diluted 1:50; Dako, Glostrup, Denmark). The adjacent sections were also stained by the Gallyas-Braak method, which has been reported to be NFT-specific [20].

## Results

### Binding affinity for synthetic A $\beta$ and tau fibrils

To characterize the binding properties of THK-523, PiB, BF-227 and FDDNP, in vitro radioligand binding assays for synthetic A $\beta_{42}$  and truncated tau construct (K18 $\Delta$ K280) fibrils were performed under the same experimental conditions. Truncated tau construct (K18 $\Delta$ K280) consists of the four repeat regions (244–372) but lacking lysine 280 ( $\Delta$ K280) observed in FTLD-17 familial mutation.

**Table 1** Demographics of brain samples used in this study

Brain no.	Age (years)	Sex	Post-mortem interval (h)
AD1	76	F	16
AD2	82	F	17
AD3	92	F	8.5

K18ΔK280 tau aggregates exhibit the similar characteristic as PHF-tau from AD brain [21]. In addition, K18ΔK280 tau forms aggregates quickly without cofactor such as heparin [22]. Thus, we used K18ΔK280 fibrils for the in vitro binding assays. Our analysis indicated that [<sup>18</sup>F]THK-523 had a higher binding affinity for tau fibrils ( $K_{D1} = 1.99 \pm 0.21$  nM,  $B_{max1} = 1.22 \pm 0.24$  pmol THK-523/nmol K18ΔK280-tau) than for Aβ<sub>42</sub> fibrils ( $K_{D1} = 30.3 \pm 3.91$  nM,  $B_{max1} = 12.6 \pm 0.45$  pmol THK-523/nmol Aβ<sub>42</sub>), which was similar to previously published data [12]. On the other hand, [<sup>3</sup>H]PiB bound to Aβ<sub>42</sub> fibrils with high affinity ( $K_{D1} = 0.84 \pm 0.18$  nM,  $B_{max1} = 0.44 \pm 0.07$  pmol PiB/nmol Aβ<sub>42</sub>). [<sup>3</sup>H]PiB also showed two binding sites for K18ΔK280-tau fibrils, but with a lower affinity ( $K_{D1} = 6.39 \pm 1.63$  nM,  $B_{max1} = 1.38 \pm 0.48$  pmol PiB/nmol K18ΔK280) than [<sup>18</sup>F]THK-523. [<sup>18</sup>F]BF-227 showed a high binding affinity for Aβ<sub>42</sub> fibrils ( $K_{D1} = 1.72 \pm 0.83$  nM,  $B_{max1} = 0.50 \pm 0.14$  pmol BF-227/nmol Aβ<sub>42</sub>), similar to our previous report [23], but showed a lower affinity for tau fibrils ( $K_D = 30.2 \pm 2.29$  nM,  $B_{max} = 10.7 \pm 0.24$  pmol BF-227/nmol K18ΔK280-tau). [<sup>18</sup>F]BF-227 had an approximately 20-fold higher affinity for the first class of Aβ<sub>42</sub> binding sites compared with tau fibrils. Only one class of [<sup>18</sup>F]FDDNP binding site was identified on the Aβ<sub>42</sub> ( $K_D = 5.52 \pm 1.97$  nM,  $B_{max} = 0.277 \pm 0.06$  pmol FDDNP/nmol Aβ<sub>42</sub>) and K18ΔK280 tau fibrils ( $K_D = 36.7 \pm 11.6$  nM,  $B_{max} = 2.14 \pm 0.46$  pmol FDDNP/nmol K18ΔK280-tau). These results suggest that [<sup>18</sup>F]FDDNP binds Aβ<sub>42</sub> fibrils with lower affinity than [<sup>3</sup>H]PiB and [<sup>18</sup>F]BF-227. Furthermore, [<sup>18</sup>F]FDDNP had an approximately sevenfold higher affinity for Aβ<sub>42</sub> fibrils than for tau fibrils. These binding profiles are significantly different from that of [<sup>18</sup>F]THK-523 (Table 2).

#### In vitro autoradiography of human brain sections

To further assess the binding selectivity of [<sup>18</sup>F]THK-523, autoradiographic images of the frontal (Fig. 2) and medial temporal (Fig. 3) brain sections from three AD patients, using [<sup>18</sup>F]THK-523, [<sup>11</sup>C]PiB and [<sup>11</sup>C]BF-227, were compared. While Aβ plaques in the frontal grey matter were

labelled with [<sup>11</sup>C]PiB (Fig. 2a–c) and [<sup>11</sup>C]BF-227 (Fig. 2g–i), the binding of [<sup>18</sup>F]THK-523 in the frontal grey matter (Fig. 2m–o) was considerably lower. In the medial temporal brain sections, [<sup>11</sup>C]PiB (Fig. 3a–c) and [<sup>11</sup>C]BF-227 (Fig. 3g–i) did not accumulate in the hippocampal CA1 area, whereas [<sup>18</sup>F]THK-523 (Fig. 3m–o) did accumulate in this area (Fig. 3m–o). The presence of a high density of tau and a low density of Aβ in this area was confirmed by immunohistochemistry (Fig. 3d–f, j–l). Furthermore, the band-like distribution of [<sup>18</sup>F]THK-523 in the inner layer of the temporal grey matter was similar to the distribution of tau (Fig. 3j–l). In the high-magnification images of case AD3 (Fig. 3p–v), the distribution of [<sup>18</sup>F]THK-523 closely resembled Gallyas silver staining and tau immunostaining. [<sup>18</sup>F]THK-523 binding was observed in the areas showing a high density of NFTs in the hippocampal CA1, the layer pre-α and pri-α in the entorhinal cortex (ERC) (Fig. 3p, q, r, t). Intriguingly, [<sup>18</sup>F]THK-523 labelling in the layer pre-α of the ERC corresponded to Gallyas silver staining better than tau immunostaining, suggesting the preferential binding of [<sup>18</sup>F]THK-523 to extracellular tau deposits that were clearly visualized by Gallyas silver staining [25]. In contrast to [<sup>18</sup>F]THK-523, the distribution of [<sup>11</sup>C]PiB was similar to that of Aβ immunohistochemistry (Fig. 3q, u, v). [<sup>11</sup>C]PiB binding corresponded to the formation of amyloid in the parvopyramidal layer of the presubicular area and in the layers pre-β and pre-γ of the ERC (Fig. 3s, v) [26].

#### Discussion

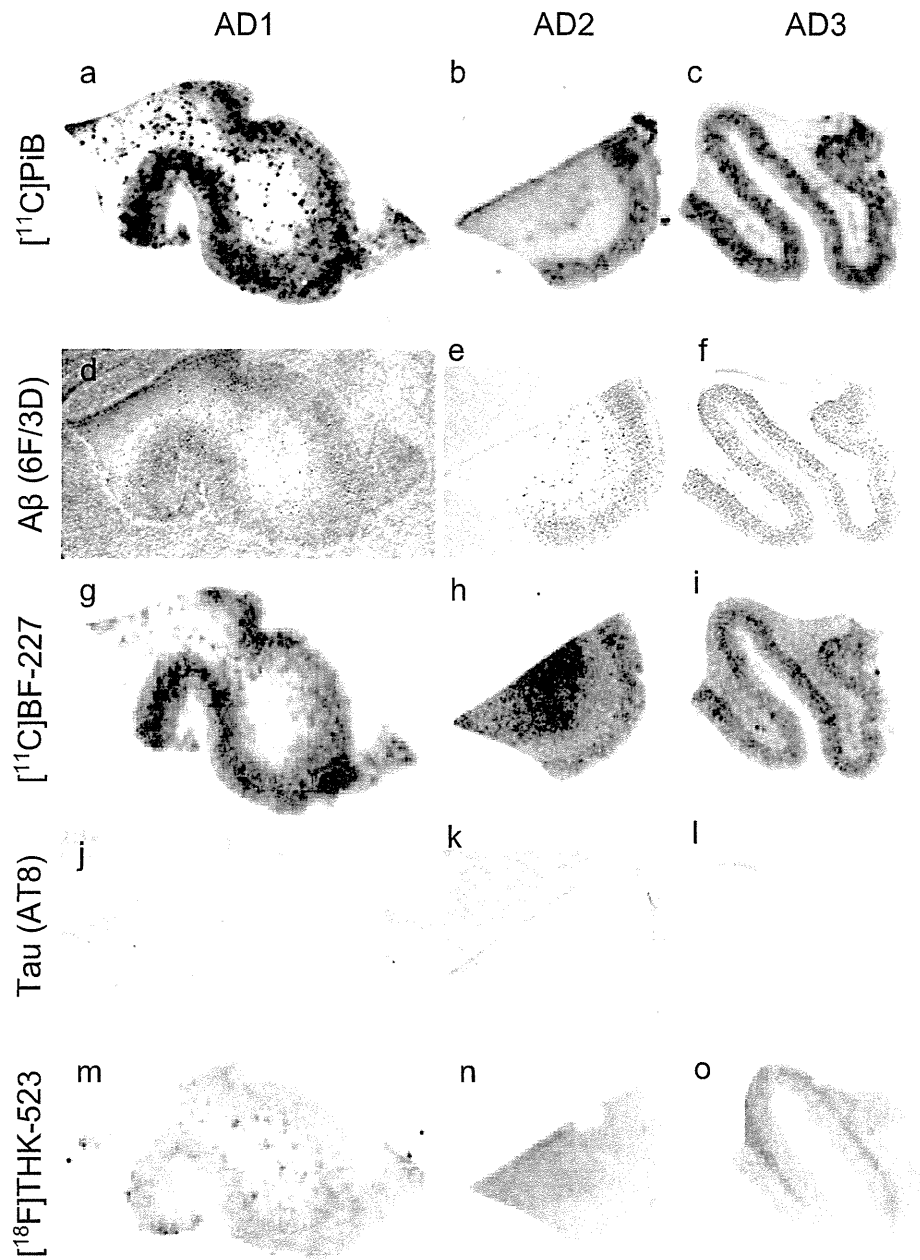
In the study reported here, we for the first time directly compared the binding properties of the novel quinoline derivative THK-523 and other amyloid PET probes. Our data suggest the potential utility of THK-523 for the selective detection of PHF-tau in the living human brain, which has not previously been achieved. The autoradiographic images of sections from AD brains revealed that [<sup>18</sup>F]THK-523 successfully labelled PHF-tau deposits but did not label Aβ deposits in the frontal and temporal cortices. These findings suggest that [<sup>18</sup>F]THK-523 is a promising

**Table 2**  $K_D$  and  $B_{max}$  values of [<sup>3</sup>H]PiB, [<sup>18</sup>F]BF-227, [<sup>18</sup>F]FDDNP and [<sup>18</sup>F]THK-523 for K18ΔK280-tau and Aβ<sub>42</sub> fibrils

Compound	K18ΔK280 fibrils				Aβ <sub>42</sub> fibrils			
	$K_{D1}$	$B_{max1}$	$K_{D2}$	$B_{max2}$	$K_{D1}$	$B_{max1}$	$K_{D2}$	$B_{max2}$
[ <sup>18</sup> F]THK-523	1.99±0.21	1.22±0.24	50.7±2.73	4.55±0.74	30.3±3.91	12.6±0.45	–	–
[ <sup>18</sup> F]BF-227	30.2±2.29	10.7±0.24	–	–	1.72±0.83	0.50±0.14	56.1±25.1	13.4±4.37
[ <sup>18</sup> F]FDDNP	36.7±11.6	2.14±0.46	–	–	5.52±1.97	0.277±0.06	–	–
[ <sup>3</sup> H]PiB	6.39±1.63	1.38±0.48	304±77.4	20.6±11.2	0.84±0.18	0.44±0.07	60.6±8.32	26.1±8.57

$K_D$  values are in nanomoles, and  $B_{max}$  values are in picomoles compound per nanomole fibrils ( $n=3$ ).

**Fig. 2** Comparison of [ $^{11}\text{C}$ ]PiB, [ $^{11}\text{C}$ ]BF-227 and [ $^{18}\text{F}$ ]THK-523 autoradiography with the A $\beta$  and tau immunostaining in sections of the frontal brain from three patients with AD (AD1, AD2, AD3). Both [ $^{11}\text{C}$ ]PiB (a–c) and [ $^{11}\text{C}$ ]BF-227 (g–i) showed dense accumulation in the grey matter, closely resembling the pattern of A $\beta$  immunohistochemistry using the 6F/3D antibody (d–f). [ $^{18}\text{F}$ ]THK-523 (m–o) did not accumulate in the grey matter, which was correlated with no marked staining with anti-tau antibody AT8 (j–l)



candidate as a tau imaging tracer, and could also be a lead compound for future development of tau-selective radiotracers. We speculate that [ $^{18}\text{F}$ ]THK-523 would show retention in tau-rich brain regions if administered to AD patients. However, the specific signal of [ $^{18}\text{F}$ ]THK-523 might be lower than those of PiB and BF-227 owing to the lower amount of tau deposits in the neocortex of AD patients [27]. Further compound optimization may be required to achieve higher contrast imaging of PHF-tau deposits.

In *in vitro* saturation binding studies [ $^{18}\text{F}$ ]THK-523 bound with higher affinity to tau fibrils ( $K_{\text{D}1}$  1.99 nM) than to A $\beta_{42}$  fibrils ( $K_{\text{D}1}$  30.3 nM), whereas PiB and BF-227 showed the

opposite binding characteristics. [ $^3\text{H}$ ]PiB bound with higher affinity to A $\beta_{42}$  fibrils ( $K_{\text{D}1}$  0.84 nM) than to tau fibrils ( $K_{\text{D}1}$  6.39 nM), similar to previous reports [7, 28, 29], and [ $^{18}\text{F}$ ]BF-227 had more than a tenfold higher affinity for A $\beta_{42}$  fibrils ( $K_{\text{D}1}$  1.72 nM) than for tau fibrils (K18 $\Delta$ K280;  $K_{\text{D}1}$  30.2 nM). Autoradiographic images of sections of AD brain revealed that [ $^{11}\text{C}$ ]PiB and [ $^{11}\text{C}$ ]BF-227 accumulated in the grey matter of the neocortex, which closely resembled the staining pattern of A $\beta$  immunohistochemistry. A previous study suggested that [ $^3\text{H}$ ]PiB labelled NFTs at tracer concentrations usually achieved during a PET scan [13]. However, another study showed no binding of the PiB derivative [ $^3\text{H}$ ]BTA-1 to

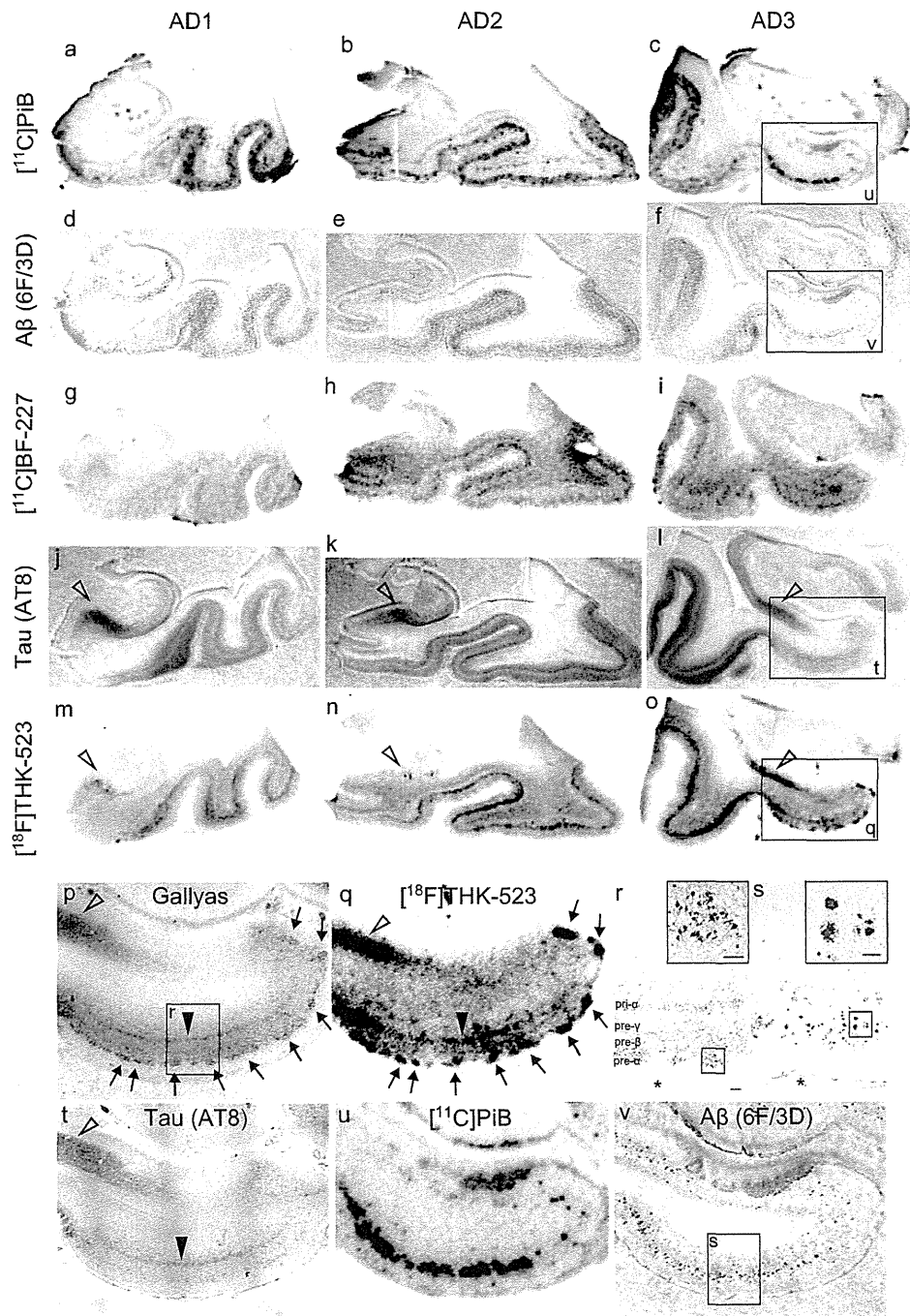


**Fig. 3** Comparison of [ $^{11}\text{C}$ ]PiB, [ $^{11}\text{C}$ ]BF-227 and [ $^{18}\text{F}$ ]THK-523 autoradiography with A $\beta$  and tau immunostaining images in sections of the medial temporal brain from three patients with AD (AD1, AD2, AD3). [ $^{11}\text{C}$ ]PiB (a–c) and [ $^{11}\text{C}$ ]BF-227 (g–i) do not accumulate in the hippocampal CA1 area which contains a low density of A $\beta$  (d–f). In contrast, accumulation of [ $^{18}\text{F}$ ]THK-523 is observed in the hippocampal CA1 area (m–o, arrowheads), which closely resembles AT8 immunoreactivity (j–l, arrowheads). In addition, the band-like labelling pattern of [ $^{18}\text{F}$ ]THK-523 in the inner layer of temporal cortex (m–o) is closely similar to that of AT8 immunostaining (j–l). p–v High magnification images of the medial temporal sections from patient AD3. Many clusters of [ $^{18}\text{F}$ ]THK-523 binding in the ERC are consistent

with Gallyas silver staining (p, q, arrows). r Close-up image from p. Numerous NFTs are located in the layer pre- $\alpha$  of the ERC (r inset). The band-like distribution of [ $^{18}\text{F}$ ]THK-523 in the layer pri- $\alpha$  of the ERC also resembles the labelling pattern of Gallyas silver staining (p, filled arrowhead) as well as AT8 immunoreactivity (t, filled arrowhead). [ $^{11}\text{C}$ ]PiB binding (u) is also present in the ERC, but obviously different from [ $^{18}\text{F}$ ]THK-523 binding (q) and similar to the 6F/3D immunostaining pattern (v). Lake-like amyloid in the presubicular region (v) is labelled with [ $^{11}\text{C}$ ]PiB, but not with [ $^{18}\text{F}$ ]THK-523. s Close-up image from v. A $\beta$  plaques (s inset) located in the layer pre- $\beta$  and pre- $\gamma$  are intensely labelled with [ $^{11}\text{C}$ ]PiB (u). Asterisks in r and s denote the same large blood vessel. Scale bar 100  $\mu\text{m}$



plaque-free and NFT-rich ERC homogenates, despite the high amount of [ $^3\text{H}$ ]BTA-1 binding to frontal cortex homogenates containing high levels of neuritic plaques [30]. Autoradiographic and immunohistochemical analyses indicated that PiB predominantly binds to senile plaques but not to NFTs. These findings are consistent with the findings from clinical PiB-PET studies showing no remarkable PiB retention in the medial temporal cortex of AD patients [7].

Another radiotracer, [ $^{18}\text{F}$ ]FDDNP, has been reported to detect A $\beta$  and tau pathological lesions in AD patients [3]. Previous clinical PET studies have shown higher cortical uptake of [ $^{18}\text{F}$ ]FDDNP in the lateral and medial temporal lobes of AD subjects [3, 5]. Furthermore, a multitracer PET study of [ $^{11}\text{C}$ ]PiB and [ $^{18}\text{F}$ ]FDDNP has shown significant retention of FDDNP in the medial temporal cortex, albeit no remarkable retention of PiB in the same region [31]. However, in vitro binding studies have shown the limited binding affinity of [ $^3\text{H}$ ]FDDNP to AD pathological lesions [24], and a previous autoradiographic analysis has suggested that [ $^3\text{H}$ ]FDDNP does not significantly label any region in AD brain [24]. Previous in vitro binding studies additionally showed the binding affinity of FDDNP for A $\beta_{40}$  fibrils ( $K_D$  0.12, 85 nM) [19, 24], but the binding affinity for tau fibrils was not reported. Here, we showed that the binding affinity of [ $^{18}\text{F}$ ]FDDNP for tau fibrils ( $K_{D1}$  36.7 nM) was similar to that of [ $^{18}\text{F}$ ]BF-227 ( $K_{D1}$  30.2 nM), but much higher than that of [ $^{18}\text{F}$ ]THK-523 ( $K_{D1}$  1.99 nM).

In conclusion, the binding profiles of [ $^{18}\text{F}$ ]THK-523, [ $^{11}\text{C}$ ]PiB, [ $^{18}\text{F}$ ]BF-227, and [ $^{18}\text{F}$ ]FDDNP were compared using in vitro saturation binding assays and autoradiography of sections of AD brain. These data suggest that [ $^{18}\text{F}$ ]THK-523 shows a binding preference for tau protein fibrils. Therefore, [ $^{18}\text{F}$ ]THK-523 is a candidate as a radiotracer to identify tau protein deposits and a lead compound for future tracer development. Ongoing clinical trials will clarify the clinical utility of this tracer and its derivatives for tau imaging in vivo.

**Acknowledgments** This study was supported by the Industrial Technology Research Grant Program of the NEDO in Japan, Health and Labor Sciences Research Grants from the Ministry of Health, Labor, and Welfare of Japan, and Grant-in-Aid for Scientific Research (B) (23390297).

## References

- Nordberg A, Rinne JO, Kadir A, Langstrom B. The use of PET in Alzheimer disease. *Nat Rev Neurol*. 2010;6:78–87. doi:10.1038/nrneurol.2009.217.
- Furumoto S, Okamura N, Iwata R, Yanai K, Arai H, Kudo Y. Recent advances in the development of amyloid imaging agents. *Curr Top Med Chem*. 2007;7:1773–89.
- Shoghi-Jadid K, Small GW, Agdeppa ED, Kepe V, Ercoli LM, Siddarth P, et al. Localization of neurofibrillary tangles and beta-amyloid plaques in the brains of living patients with Alzheimer disease. *Am J Geriatr Psychiatry*. 2002;10:24–35.
- Mathis CA, Wang Y, Holt DP, Huang GF, Debnath ML, Klunk WE. Synthesis and evaluation of  $^{11}\text{C}$ -labeled 6-substituted 2-arylbenzothiazoles as amyloid imaging agents. *J Med Chem*. 2003;46:2740–54. doi:10.1021/jm030026b.
- Klunk WE, Engler H, Nordberg A, Wang Y, Blomqvist G, Holt DP, et al. Imaging brain amyloid in Alzheimer's disease with Pittsburgh Compound-B. *Ann Neurol*. 2004;55:306–19. doi:10.1002/ana.20009.
- Kudo Y, Okamura N, Furumoto S, Tashiro M, Furukawa K, Maruyama M, et al. 2-(2-[2-Dimethylaminothiazol-5-yl]ethenyl)-6-(2-[fluoro]ethoxy)benzoxazole: a novel PET agent for in vivo detection of dense amyloid plaques in Alzheimer's disease patients. *J Nucl Med*. 2007;48:553–61.
- Ikonomic MD, Klunk WE, Abrahamson EE, Mathis CA, Price JC, Tsopelas ND, et al. Post-mortem correlates of in vivo PiB-PET amyloid imaging in a typical case of Alzheimer's disease. *Brain*. 2008;131:1630–45. doi:10.1093/brain/awn016.
- Sperling RA, Aisen PS, Beckett LA, Bennett DA, Craft S, Fagan AM, et al. Toward defining the preclinical stages of Alzheimer's disease: recommendations from the National Institute on Aging-Alzheimer's Association workgroups on diagnostic guidelines for Alzheimer's disease. *Alzheimers Dement*. 2011;7:280–92. doi:10.1016/j.jalz.2011.03.003.
- Jack Jr CR, Knopman DS, Jagust WJ, Shaw LM, Aisen PS, Weiner MW, et al. Hypothetical model of dynamic biomarkers of the Alzheimer's pathological cascade. *Lancet Neurol*. 2010;9:119–28. doi:10.1016/S1474-4422(09)70299-6.
- Pike KE, Savage G, Villemagne VL, Ng S, Moss SA, Maruff P, et al. Beta-amyloid imaging and memory in non-demented individuals: evidence for preclinical Alzheimer's disease. *Brain*. 2007;130:2837–44. doi:10.1093/brain/awn238.
- Okamura N, Suemoto T, Furumoto S, Suzuki M, Shimadzu H, Akatsu H, et al. Quinoline and benzimidazole derivatives: candidate probes for in vivo imaging of tau pathology in Alzheimer's disease. *J Neurosci*. 2005;25:10857–62. doi:10.1523/JNEUROSCI.1738-05.2005.
- Fodero-Tavoletti MT, Okamura N, Furumoto S, Mulligan RS, Connor AR, McLean CA, et al. 18F-THK523: a novel in vivo tau imaging ligand for Alzheimer's disease. *Brain*. 2011;134:1089–100. doi:10.1093/Brain/Awr038.
- Lockhart A, Lamb JR, Osredkar T, Sue LI, Joyce JN, Ye L, et al. PiB is a non-specific imaging marker of amyloid-beta (A $\beta$ ) peptide-related cerebral amyloidosis. *Brain*. 2007;130:2607–15. doi:10.1093/brain/awn191.
- Burack MA, Hartlein J, Flores HP, Taylor-Reinwald L, Perlmutter JS, Cairns NJ. In vivo amyloid imaging in autopsy-confirmed Parkinson disease with dementia. *Neurology*. 2010;74:77–84. doi:10.1212/WNL.0b013e318181c7da8e.
- Clark CM, Schneider JA, Bedell BJ, Beach TG, Bilker WB, Mintun MA, et al. Use of florbetapir-PET for imaging beta-amyloid pathology. *JAMA*. 2011;305:275–83. doi:10.1001/jama.2010.2008.
- Wong DF, Moghekar AR, Rigamonti D, Brasic JR, Rousset O, Willis W, et al. An in vivo evaluation of cerebral cortical amyloid with [(18F)]Flutemetamol using positron emission tomography compared with parietal biopsy samples in living normal pressure hydrocephalus patients. *Mol Imaging Biol*. 2012. doi:10.1007/s11307-012-0583-x.
- Maeda J, Ji B, Irie T, Tomiyama T, Maruyama M, Okauchi T, et al. Longitudinal, quantitative assessment of amyloid, neuroinflammation, and anti-amyloid treatment in a living mouse model of Alzheimer's disease enabled by positron emission tomography. *J Neurosci*. 2007;27:10957–68. doi:10.1523/JNEUROSCI.0673-07.2007.

18. Manook A, Yousefi BH, Willuweit A, Platzer S, Reder S, Voss A, et al. Small-animal PET imaging of amyloid-beta plaques with [<sup>11</sup>C]PiB and its multi-modal validation in an APP/PS1 mouse model of Alzheimer's disease. *PLoS One*. 2012;7:e31310. doi:10.1371/journal.pone.0031310.
19. Agdeppa ED, Kepe V, Liu J, Flores-Torres S, Satyamurthy N, Petric A, et al. Binding characteristics of radiofluorinated 6-dialkylamino-2-naphthylethylidene derivatives as positron emission tomography imaging probes for beta-amyloid plaques in Alzheimer's disease. *J Neurosci*. 2001;21:RC189.
20. Gallyas F. Silver staining of Alzheimer's neurofibrillary changes by means of physical development. *Acta Morphol Acad Sci Hung*. 1971;19:1–8.
21. Barghorn S, Davies P, Mandelkow E. Tau paired helical filaments from Alzheimer's disease brain and assembled in vitro are based on beta-structure in the core domain. *Biochemistry*. 2004;43:1694–703. doi:10.1021/bi0357006.
22. von Bergen M, Barghorn S, Muller SA, Pickhardt M, Biemat J, Mandelkow EM, et al. The core of tau-paired helical filaments studied by scanning transmission electron microscopy and limited proteolysis. *Biochemistry*. 2006;45:6446–57. doi:10.1021/bi052530j.
23. Fodero-Tavoletti MT, Mulligan RS, Okamura N, Furumoto S, Rowe CC, Kudo Y, et al. In vitro characterisation of BF227 binding to alpha-synuclein/Lewy bodies. *Eur J Pharmacol*. 2009;617:54–8. doi:10.1016/j.ejphar.2009.06.042.
24. Thompson PW, Ye L, Morgenstern JL, Sue L, Beach TG, Judd DJ, et al. Interaction of the amyloid imaging tracer FDDNP with hallmark Alzheimer's disease pathologies. *J Neurochem*. 2009;109:623–30. doi:10.1111/j.1471-4159.2009.05996.x.
25. Braak E, Braak H, Mandelkow EM. A sequence of cytoskeleton changes related to the formation of neurofibrillary tangles and neuropil threads. *Acta Neuropathol*. 1994;87:554–67.
26. Thal DR, Rub U, Schultz C, Sassin I, Ghebremedhin E, Del Tredici K, et al. Sequence of Abeta-protein deposition in the human medial temporal lobe. *J Neuropathol Exp Neurol*. 2000;59:733–48.
27. Villemagne VL, Furumoto S, Fodero-Tavoletti M, Harada R, Mulligan RS, Kudo Y, et al. The challenges of tau imaging. *Future Neurol*. 2012;7:409–21. doi:10.2217/fnl.12.34.
28. Fodero-Tavoletti MT, Smith DP, McLean CA, Adlard PA, Barnham KJ, Foster LE, et al. In vitro characterization of Pittsburgh compound-B binding to Lewy bodies. *J Neurosci*. 2007;27:10365–71. doi:10.1523/JNEUROSCI.0630-07.2007.
29. Klunk WE, Lopresti BJ, Ikonomic MD, Lefterov IM, Koldamova RP, Abrahamson EE, et al. Binding of the positron emission tomography tracer Pittsburgh compound-B reflects the amount of amyloid-beta in Alzheimer's disease brain but not in transgenic mouse brain. *J Neurosci*. 2005;25:10598–606. doi:10.1523/JNEUROSCI.2990-05.2005.
30. Klunk WE, Wang Y, Huang GF, Debnath ML, Holt DP, Shao L, et al. The binding of 2-(4'-methylaminophenyl)benzothiazole to post-mortem brain homogenates is dominated by the amyloid component. *J Neurosci*. 2003;23:2086–92.
31. Shin J, Lee SY, Kim SH, Kim YB, Cho SJ. Multitracer PET imaging of amyloid plaques and neurofibrillary tangles in Alzheimer's disease. *Neuroimage*. 2008;43:236–44. doi:10.1016/j.neuroimage.2008.07.022.